The equilibrium intrinsic crystal–liquid interface of colloids

Jessica Hernández-Guzmán and Eric R. Weeks[1]

Department of Physics, Emory University, Atlanta, GA 30322

We use confocal microscopy to study an equilibrated crystal–liquid interface in a colloidal suspension. Capillary waves roughen the surface, but locally the intrinsic interface is sharply defined. We use local measurements of the structure and dynamics to characterize the intrinsic interface, and different measurements find slightly different widths of this interface. In terms of the particle diameter d, this width is either $1.5d$ (based on structural information) or $2.4d$ (based on dynamics), both not much larger than the particle size. This work is the first direct experimental visualization of an equilibrated crystal–liquid interface.

surface tension | capillary waves | confocal microscopy

The interface between crystal and liquid phases of a material governs phenomena such as wetting, lubrication, and crystal nucleation (1, 2). Interfaces are poorly defined at the atomic level: Capillary waves cause fluctuations in the interface position (3–6), and locally the structure varies in a smooth way from ordered to disordered (2). Existing literature makes a distinction between the intrinsic interface (presumed to be sharp) (3), and the observed surface blurred by capillary waves (4, 7). The standard equilibrium interface profile is well defined and contains fluctuations at all length and time scales, due to these capillary waves. Because of the rapid time scales of capillary-wave fluctuations, along with the small length scales at the interface, it is difficult to study these interfaces directly (1). Thus, computer simulations provide useful information about model crystal–liquid interfaces, such as hard-sphere systems (2, 8, 9) and Lennard–Jones systems (10, 11).

Recently, crystal–liquid interfaces were directly studied in colloidal suspensions by using confocal microscopy (6, 12). Colloids are systems of solid particles in a liquid and are a good model system for phase transitions (5, 6, 13, 14). Microscopy allows direct observation of structure and dynamics of the colloidal particles (15). However, the previous experiments focused on nonequilibrium cases where samples were crystallizing and did not provide data on equilibrium interfaces, such as those studied by simulation (2, 8–10, 16). Furthermore, these experiments did not examine the intrinsic interface, perhaps because they were nonequilibrium studies, and thus crystalline particles were present in the "liquid" side and vice versa, which confuse the structure near the interface.

In this work, we present confocal microscope observations of an equilibrated colloidal crystal–liquid interface. By following the positions of several thousand colloidal particles on both sides of the interface, we directly visualize the interface. An example of our data is shown in Fig. 1*A*, where blue particles are crystalline and yellow/red particles are liquid-like. This interface has a low surface tension, and we see capillary waves. We are able to remove the influence of these capillary waves from the data and measure the intrinsic surface profile. In particular, we find that capillary waves cause an apparent broadening of the surface, but the structure of the intrinsic surface is characterized by a width of only $1.5d$ (in terms of the particle diameter d). This is the first direct experimental visualization of an equilibrated interface. A precise definition of the intrinsic interface has not

been made before, and we show that several plausible definitions give slightly different results.

Our colloidal sample is described in *Materials and Methods*. Here, we briefly note that in our solvent the colloidal particles have a slight charge. Experimentally, we observe that the freezing transition volume fraction is at $\phi_{\text{freeze}} = 0.43$, and the melting transition is at $\phi_{\text{melt}} = 0.49$, to be compared with the hard-sphere values of $\phi_{\text{freeze}} = 0.494$ and $\phi_{\text{melt}} = 0.545$. Our measured values are similar to those seen for other experiments with similar colloidal samples (12).

Results

At each time step, we determine the crystalline region by using the method of bond-order parameters (6, 12, 17, 18). To do this, each particle i at each time is characterized by a normalized order parameter $\hat{\mathbf{q}}_l(i)$ with $(2l + 1)$ complex components

$$\hat{q}_{lm}(i) = \frac{1}{\mathcal{N}B(i)} \sum_{j=1}^{B(i)} Y_{lm}(\hat{r}_{ij}),\qquad [\mathbf{1}]$$

where $\mathcal{N}$ is a normalization factor, such that $\sum_m \hat{q}_{lm}(i)\hat{q}_{lm}^*(i) = 1$, $B(i)$ is the number of neighbors of particle i, $\hat{r}_{ij}$ is the unit vector pointing from particle i to its jth neighbor, and Y_{lm} is a spherical harmonic function. Following prior work, we use $l = 6$ (12, 18). The neighbors of a particle are defined as those with centers separated by $<1.41d$, which corresponds to the first minimum of the pair correlation function $g(r)$ for the liquid region. Two neighboring particles are termed "ordered neighbors" if the complex inner product $\sum_m \hat{q}_{lm}(i) \hat{q}_{lm}^*(j)$ exceeds a threshold value of 0.5. For each particle, the number of ordered neighbors N_o is determined. Following the usual convention, particles with $N_o \geq 8$ are classed as crystalline particles, and the other particles are liquid-like particles (18). The advantages of using bond-order parameters are that they are local measures of order, are somewhat insensitive to variations in the number of neighbors each particle has, and do not depend on the specific type of crystal (17, 18).

Fig. 1*A* shows a snapshot of the sample, colored according to the bond-order parameter method. The crystalline side of the interface (blue particles) is composed of hexagonal layers in random stacking [a mixture of face-centered-cubic stacking (*abcabc*..) and hexagonal-close-packed stacking (*ababab*..)]. This stacking is similar to that seen in growing colloidal crystallites (12). In particular, the data shown in this article are for a sample where nine hexagonal layers are imaged, with stacking *abacbcbac*. Two other regions of this sample were imaged and the results presented below do not vary in any significant way.

Typically, between two different phases, there will always exist a surface energy defining the energetic cost of maintaining the interface. For fluid–fluid interfaces, this is also known as the
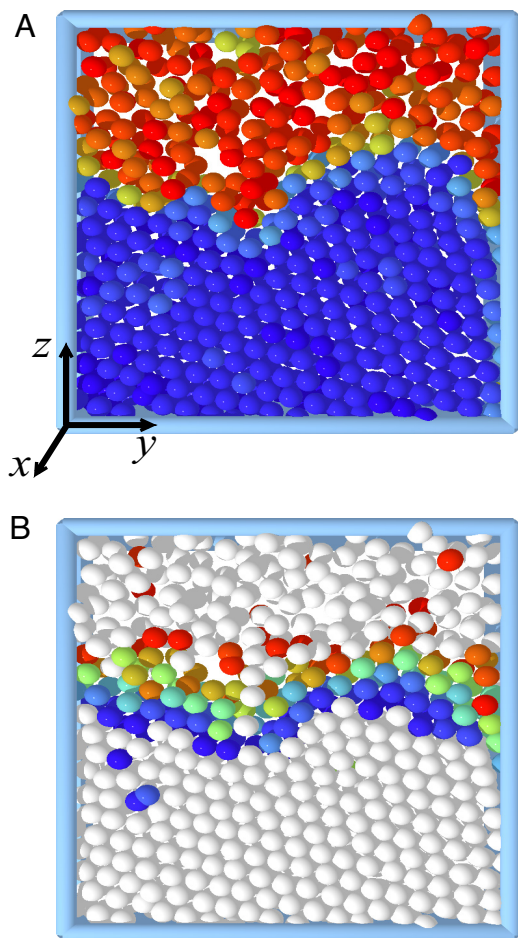
Fig. 1. Pictures showing the crystal–liquid interface. (*A*) Picture of the liquid–crystal interface showing a slice that is two crystalline layers thick (4.8 μm). Particles are colored according to the number of ordered neighbors they have, N_o. Blue particles have $N_o \geq 8$, and darker blue indicates higher N_o. Yellow, orange, and red particles have $N_o < 8$, with red particles having $N_o = 0$, and the brightest yellow particles having $N_o = 7$. The image has been slightly rotated (by 3° around an axis parallel to gravity) to view the crystalline particles in-plane. (*B*) Here the particles are colored according to how much time they spend as "crystalline" particles (with $N_o \geq 8$). White particles spend all of their time as crystalline or liquid-like, and the colored particles fluctuate over the ≈1-hr experiment. Blue particles spend nearly all their time as crystalline, light green corresponds to those which spend half their time in each state, and red particles spend nearly all their time as liquid-like. Although the coloring is based on the time average of the data, the positions are considered at the same time as those shown in *A*.

surface tension, although the concept is relevant for solid–liquid interfaces as well [for example, in nucleation of crystals (12)]. For a hard-sphere system, this surface energy is entropic in origin, reflecting the difficulty of packing particles at the interface. Right at the interface, particles can pack neither optimally for the crystal state nor optimally for the liquid state, thus resulting in an entropic penalty that gives rise to a surface tension. In our experiment, the interface shown in Fig. 1 is rough and varies in time due to surface capillary waves. Because the surface energy is not extremely large compared with $k_B T$ (the thermal energy, based on the temperature T and Boltzmann's constant k_B), thermal fluctuations allow these capillary waves to be observed in our experiment. The temporal variability of the sample is indicated in Fig. 1*B*, which colors only the particles that we observe to spend some time in both crystalline and liquid structures for the duration of our experiment (3,750 s). As can
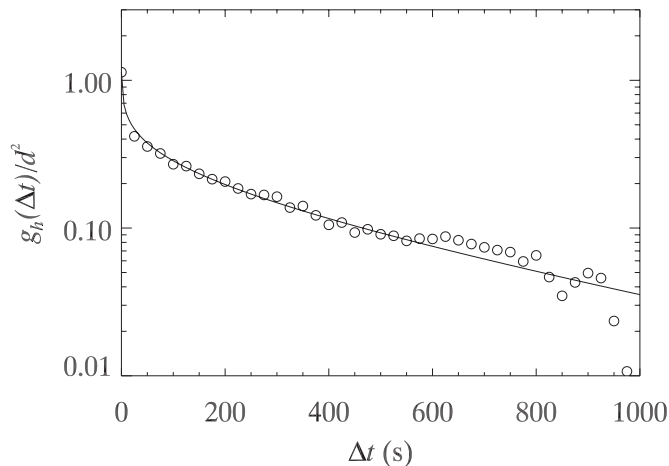
Fig. 2. Interfacial height correlation function. The circles show the temporal correlation function of interface position, averaged over *x* and *y* (Eq. **2**). The line is a fit to Eq. **5**, with interfacial stiffness $\tilde{\gamma} = 0.93$ nN/m $= 1.2\, k_B T/d^2$ and a capillary time $\tau = 750$ s. The small *k* modes give rise to the very steep drop of the correlation at short time scales, and the exact shape of the theoretical curve for $\Delta t < 25$ s depends on how the numeric integration of Eq. **5** is done.

be seen, the exact position of the interface thus fluctuates by as much as ≈4 particle diameters (in a "peak-to-peak" sense).

To determine the surface tension, we follow the procedure of ref. 5. Due to a slight purposeful density mismatch (described in *Methods and Materials*), the crystal–liquid interface is nearly parallel to the *xy* plane; we rotate the data by 15° to align the interface with the *xy* plane. Based on the new *z* axis, at each time we locate the maximum *z* position of crystalline particles as a function of *x* and *y* (coarse-grained in *x* and *y* over a distance $1.035d$, the spacing between crystalline layers, where *d* is the diameter of an individual particle), giving us the interface height $h(x, y, t)$. Although our data are only over a short spatial extent in *x* and *y* ($9d \times 24d$), we have good temporal data ($0 \leq t \leq 3{,}750$ s), and thus we calculate the temporal dynamical correlation function

$$g_h(\Delta t) = \langle [h'(x, y, t)][h'(x, y, t + \Delta t)] \rangle_{x,y,t} \qquad [2]$$

where $h'(x, y, t) = h(x, y, t) - \langle h(x, y, t) \rangle_t$ represents the fluctuations of the interface about its time-averaged position, and the angle brackets $\langle \ldots \rangle_{x,y,t}$ indicate an average over space and time. We plot this dynamic correlation function in Fig. 2 (circles). The intercept is at $g_h(\Delta t = 0) \approx 1.1d^2$; thus, the root-mean-square width of the capillary wave fluctuations is approximately *d*, as compared with the slightly larger amplitude of the peak-to-peak fluctuations seen in Fig. 1*B*.

The capillary waves are limited by the interfacial stiffness $\tilde{\gamma}$, rather than the surface tension γ (16). For a crystal–liquid interface, γ is usually anisotropic and depends on the crystal orientation. Fluctuations in the surface thus depend both on γ (related to interfacial stretching) as well as second derivatives of γ with respect to angles away from the interface normal (related to interfacial bending). The orientational average of $\tilde{\gamma}$ is the bulk surface tension γ, but measuring this requires vastly more data than we have (8, 16, 19). To extract the interfacial stiffness $\tilde{\gamma}$, we fit $g_h(\Delta t)$ by using the results of capillary wave theory (5, 20). Overdamped capillary waves with wave number *k* should decay as

$$\exp[-t(\tilde{\gamma}k + g\Delta\rho_i/k)/(2\eta)], \qquad [3]$$

with gravitational acceleration *g*, density difference $\Delta\rho_i$ (across the interface), and viscosity η (equal to the sum of the viscosities

of the two phases) (20). By equipartition, the amplitude of the Fourier component h_k of the interface displacement contributes as

$$\langle |h_k|^2 \rangle = \frac{k_B T}{\tilde{\gamma} L^2} \frac{1}{k^2 + \xi^{-2}} \qquad [4]$$

with L the lateral system size, and using the capillary length $\xi = \sqrt{\tilde{\gamma}/(g\,\Delta\rho_i)}$ (21). As in ref. 5, we define the nondimensional $\bar{k} = \xi k$, and then combine these two results to calculate the theoretical dynamic correlation function as an integral

$$gh(\Delta t) = \frac{k_B T}{2\pi\tilde{\gamma}} \int_0^\infty d\bar{k}\,\bar{k}\,\frac{\exp[-(\bar{k} + \bar{k}^{-1})\Delta t/(2\tau)]}{1 + \bar{k}^2} \qquad [5]$$

with $\tau = \xi\eta/\tilde{\gamma}$ as the capillary time, the characteristic time scale for decay of interfacial fluctuations (21). In particular, τ corresponds to the time scale for the slowest decaying wavelength, which is at the capillary length scale ξ.

We vary τ and $\tilde{\gamma}$ to find the best fit to our data, and plot this as the solid line in Fig. 2, finding excellent agreement using $\tilde{\gamma} = 1.2\ k_B T/d^2$. Our value of $\tilde{\gamma} = 1.20 \pm 0.05$ (in units of $k_B T/d^2$) is a similar order of magnitude to previously found values of γ for hard spheres, which range from 0.11 to 0.78 (8, 9, 12, 22–24). Our measured $\tilde{\gamma}$ is larger than these values of γ, perhaps due to the above-noted anisotropy of $\tilde{\gamma}$, for which we may have a stiff direction (8).

We note several limitations with our measurement of the interfacial stiffness. First, our result is calculated for one particular interface orientation, rather than averaging over many different crystal orientations. Second, the theory of refs. 5 and 21 is derived for liquid–gas interfaces, where the surface tension is isotropic. As noted above, the local interfacial stiffness is an adequate replacement for the isotropic surface tension (8). Third, the theory also assumes that both phases have a well-defined viscosity, whereas one of our phases is a colloidal crystal. The crystalline phase could be considered as a liquid with a very large viscosity, but this would then predict a very large capillary time, in contrast with our observed $\tau = 750$ s. This value is consistent with a viscosity $\eta = 50$ mPa·s $\approx 20\ \eta_0$ (compared with the solvent viscosity η_0). This value is approximately half of what could be expected for high-volume fraction colloidal samples at volume fractions $\phi = 0.43 - 0.49$ (25), given that η here represents the sum of the viscosities of the two phases. To summarize, our crystal-liquid interface has capillary waves which fluctuate in a way consistent with predictions for liquid–gas capillary waves, but interpretations of this observation should be done cautiously.

Additionally we note that the space-averaged height $\langle h(x,y,t)\rangle_{x,y}$ fluctuates but does not monotonically increase or decrease, confirming that we observe an equilibrium interface rather than a system which is crystallizing or melting. However, as can be seen in Fig. 1B, the exact interface position fluctuates only within a certain range over the duration of our experiment, precluding us from a true ensemble-averaged measurement. For a longer duration experiment, the time-averaged shaded region in Fig. 1B would presumably meander less and be more uniform across the y direction.

We now turn to the structural details of the crystal–liquid interface. As mentioned above, we rotate the data around the x axis by 15° clockwise (as seen from the view in Fig. 1), so that the crystal structure is aligned with the new z axis; see Fig. 3A Inset. We then plot the number density $d^3 n(z)$ as a function of z/d in Fig. 3A and see oscillations similar to what has been seen in experiments (6) and simulations (2, 10, 11). The smooth line in Fig. 3A is a hyperbolic tangent fit to the data. Following previous work, we define the interfacial width as the 10–90 width, where the hyperbolic tangent function goes from 10% of
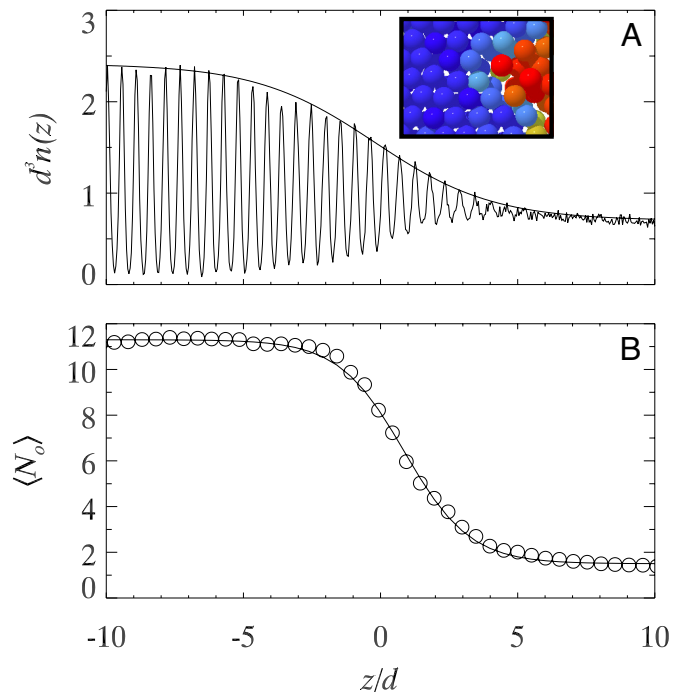

Fig. 3. Two views of the interfacial profile in the ''laboratory'' reference frame. (A) Interfacial profile showing the number density profile $d^3 n(z)$ as a function of z/d. The smooth curve is a hyperbolic tangent fit to the envelope, with 10–90 width of 9.6d. *Inset* shows the crystal orientation used to determine this curve, after the sample has been rotated slightly. (B) Bond-order profile showing the average number of ordered neighbors particles have, as a function of z/d. The dotted curve is again a hyperbolic tangent fit, with a 10–90 width of 6.1d. By definition, $\langle N_o \rangle = 8$ at $z = 0$. For both A and B, the data are time averaged over 2,000 s (80 3D images).

its value to 90% of its value. We find $W_{10-90} = 9.6d$, quite similar to what has been seen previously (2, 6). Some of this width is due to capillary waves, and some may be due to particles in the crystalline lattice (but near the interface) having larger fluctuations around their mean positions (2). We checked for this latter influence by low-pass filtering (2) the density profile of Fig. 3A and found a similar W_{10-90} width, although this width depends on the details of the filter—this filtering also shifts the halfway point of the hyperbolic tangent fit toward the liquid side by 4d. We also calculate the width based on the structural ordering, by plotting the average number of ordered neighbors $\langle N_o \rangle$ as a function of z'/d in Fig. 3B. Based on this measure, the profile is slightly sharper, with $W_{10-90} = 6.1d$; this sharpness agrees with previous results (2, 6).

However, Fig. 1 implies that measurements that average over x and y will artificially broaden the interface, given that the interface is not flat. Due to the fractal structure of the capillary waves, the interfacial width depends on the total system size. Our measured widths depend on the size of the observation region and would increase if the observed region was larger and encompassed more of the sample (7). Our data allow us a closer examination of the detailed behavior near the interface. For each particle, we calculate the distance s to the instantaneous interface position by using the procedure illustrated in Fig. 4.

To examine the transition from order to disorder, we calculate the average number of ordered neighbors $\langle N_o \rangle$ now as a function of s, and plot the result in Fig. 5A. By definition, $N_o \geq 8$ for crystalline particles and $N_o \leq 7$ for liquid-like particles, thus producing a gap in $\langle N_o \rangle$ at the interface. Fig. 5A shows that based on the ordering, the interface is quite sharp, with a width $W_{10-90} = 1.5\ d$, in contrast to the interpretation of Fig. 3. By this
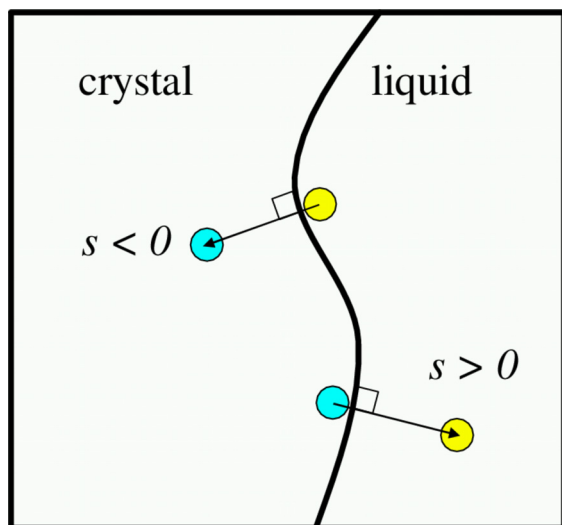
Fig. 4. Sketch defining the distance from the interface s. For crystalline particles, the distance s is found to the closest noncrystalline particle (any particle with $N_o < 8$). This distance is defined to be negative. For liquid particles, the distance s is the closest distance to the nearest crystalline particle ($N_o \geq 8$). Based on this definition, the region $-d < s < d$ is excluded, as no two particles are closer than their diameters d. Thus, we shift the distance s by $+d/2$ for crystalline particles, and by $-d/2$ for liquid particles. This shift leaves a gap of size d, reflecting that the interface truly lies between the crystalline and liquid particles.

measure, the interface is locally a sharp, well-defined interface, as has been conjectured (3, 4).

Fig. 5B shows the mobility $\Delta r/d$, measured across the interface (defined for two different time scales Δt). Here we see the interfacial width is $W_{10-90} = 2.4d$, significantly broader than that determined by the structure but still fairly narrow, supporting the interpretation of a meandering but sharp interface. On the liquid side, the mobility is still increasing for $s > d$ where $\langle N_o \rangle$ has reached the steady-state liquid value; the halfway point of the hyperbolic tangent fit is at $s = 0.2d$ for the $\Delta t = 75$ s data and at $s = 0.8d$ for the $\Delta t = 750$ s data. This result is understandable as the crystalline particles form a relatively immobile region: Thus, the more mobile liquid-like particles are slowed by proximity to the crystal, similar to a hydrodynamic "no-slip" condition. Examining the individual components of motion (Δx, Δy, Δz) we find no significant differences, indicating that the motion is isotropic, as seen in simulations (2). Although our data for $\Delta t > 750$ s are noisy, we can estimate that the diffusivity on the liquid side is $\approx 50\times$ smaller than the diffusivity in a dilute suspension, in reasonable agreement with hard-sphere simulations (2).

To examine the intrinsic density profile, we plot the number density $d^3 n(s)$ in Fig. 5C. The crystal structure has a fixed orientation and, thus, relative to the curving interface, the layers seen in Fig. 3A diminish away from the interface (the region $s < 0$). On the liquid side ($s > 0$), layering relative to the intrinsic interface is seen with two clear layers—fewer layers than the crystal side. This finding reinforces that the layering shown in Fig. 3A for the region $z > 0$ is mostly due to the uneven interface.

Discussion

Note that in this work we have studied slightly charged particles rather than ideal hard spheres. Perhaps surprisingly, our results compare reasonably well with hard-sphere simulations such as those in refs. 2, 8, 9, and 24. Thus, the influence of the charges shift the phase boundaries as noted above (a freezing volume fraction $\phi_{melt} = 0.49$ for our experiments as compared with 0.545 for hard spheres), but the charges do not seem to strongly
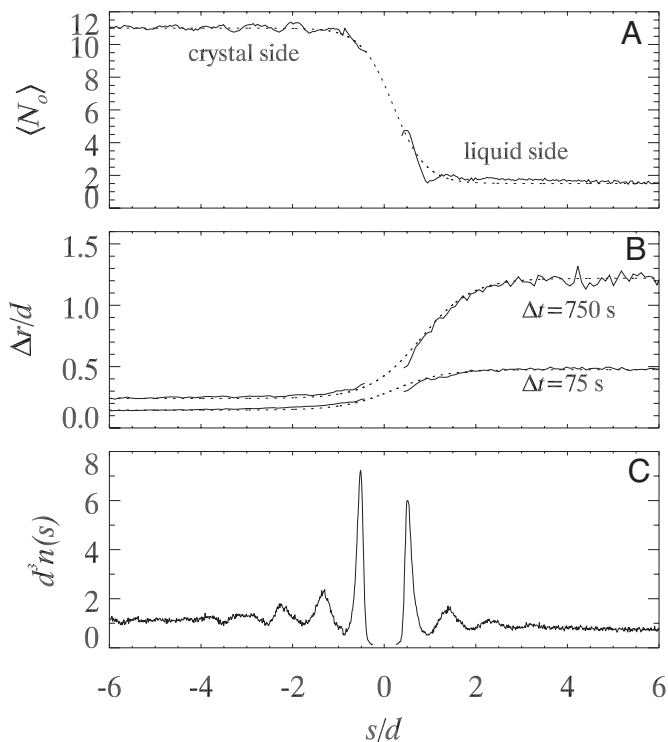

Fig. 5. Three views of the intrinsic interface profile. (*A*) Bond-order profile (solid line), showing the average number of ordered neighbors of particles as a function of s/d. s is the distance from the interface, as described in Fig. 4. The dotted line is a hyperbolic tangent fit with $W_{10-90} = 1.5d$. (*B*) Average distance Δr moved in a given Δt as indicated, as a function of s/d. The dotted lines are hyperbolic tangent fits, each with $W_{10-90} = 2.4d$. Here s is the distance measured at the particle's initial position at the start of the displacement Δr. (*C*) Nondimensional number density $d^3 n$ as a function of s/d.

modify the structure or dynamics of the interface. It is likely that particle motion is somewhat slowed due to smaller effective cage sizes (26) and thus modifies the plateau levels of Fig. 5B. However, this slowness does not seem to modify the extent of the transition region of the interface, and indeed one might expect that a long-range interaction would only broaden the interface, thus making it more striking that we observe such narrow interface widths.

We have studied the equilibrium crystal–liquid interface of a dense colloidal suspension. We observe a rough interface with width 6–10d, depending on the property examined. Capillary waves account for some of this broadening, although overall the mean-square fluctuations from capillary waves have magnitude $g_h(\Delta t = 0) \approx 1.1d^2$. Thus, there may be a base structure comprised of crystalline facets, as suggested by the darkest particles shown in Fig. 1B. These facets may be slower to rearrange, and their potential existence likely broadens the observed interface width.

We also studied the profile in the direction locally perpendicular to the rough interface, and find that this intrinsic interface is much sharper, 1.5d and 2.4d based on structure and dynamics, respectively. These results emphasize that the observed broadness of the interface is only apparent, and depends on the measurement length scales (7) and time scales (2). The underlying spatial transition from one phase to the other is quite sharp, confirming the classic picture (3, 4). Our data provide a useful test for future models of the intrinsic profile.

Materials and Methods

is a mixture of cyclohexylbromide and decalin, chosen to closely match the density and index of refraction of the particles, with viscosity $\eta_0 = 2.25$ mPa·s (27). However, we intentionally slightly density-mismatch the fluid by adding an excess of decalin, which is more dense than the particles. This mismatch lets us gravitationally induce a crystal–liquid transition within our sample chamber. Our particle–fluid density mismatch is less than $\Delta\rho \approx 5 \times 10^{-4}$ g/mL, giving us a gravitational scale height $k_B T/\Delta\rho V g > 130$ μm, using the temperature T (295 K for these experiments), the particle volume $V = \frac{\pi}{6} d^3$, and the gravitational acceleration g. In our solvent, the particles have a slight charge, shifting the freezing transition volume fractions to $\phi_{freeze} = 0.43$ and the melting transition to $\phi_{melt} = 0.49$, similar to values for other weakly charged colloidal PMMA experiments (12). The existence of the charge is also apparent from comparisons of the pair correlation function $g(r)$ taken at different volume fractions. For hard spheres, the first peak of $g(r)$ should always be at $r = d$, whereas for our samples we find the peak at $r > d$, and the peak position varies slightly with ϕ. However, this peak position is still fairly close to d; for example, in the crystalline region we find the peak at $r = 1.04d$, and in the liquid region we find the peak at $r = 1.15d$, suggesting that the charging is not too extreme (28, 29).

Our microscope sample chambers have dimensions 0.4 mm × 3 mm × 30 mm and are stored with the long dimension oriented vertically. Because of the slight density mismatch between the solvent and the particles, gravity sets up a slight concentration gradient. We let the samples equilibrate in the sample chamber for more than one month before taking data. We make one impor-

tant modification to our microscope: The microscope base is tilted 90° so that the objective lens points horizontally (30). The sample is placed on the microscope stage with the orientation kept the same as the storage conditions. Thus, we study a completely equilibrated sample at a stable crystal–liquid interface, and the direction of gravity ($-\hat{z}$) points perpendicular to the optical axis.

The particles are dyed with rhodamine 6G so that they can be viewed with a laser-scanning confocal microscope (15, 27). We acquire images of size 20 × 55 × 60 μm³ once every 25 s, where the long direction (z) is parallel to gravity. The images were taken from 20 to 40 μm away from the coverslip to avoid direct influence of the walls. As noted above, the full sample size is 0.4 × 3 × 30 mm³, where the smallest dimension is x, and the largest direction is z; thus, the imaged region is only a small volume within the sample. The 3D images are analyzed to determine particle positions with a resolution of 0.1 μm parallel to the optical axis (x) (27, 31), and a resolution of 0.05 μm perpendicular to the optical axis (y and z). Because this is a dense sample, particles do not move far between images, and thus we follow their motion by using standard particle-tracking techniques (31).

1. Kaplan WD, Kauffmann Y (2006) Structural order in liquids induced by interfaces with crystals. *Annu Rev Mater Res* 36:1–48.
2. Davidchack RL, Laird BB (1998) Simulation of the hard-sphere crystal–melt interface. *J Chem Phys* 108:9452–9462.
3. Buff FP, Lovett RA, Stillinger FH (1965) Interfacial density profile for fluids in the critical region. *Phys Rev Lett* 15:621–623.
4. Muller M, Munster G (2005) Profile and width of rough interfaces. *J Stat Phys* 118:669–686.
5. Aarts DG, Schmidt M, Lekkerkerker HN (2004) Direct visual observation of thermal capillary waves. *Science* 304:847–850.
6. Dullens RPA, Aarts, DGAL, Kegel WK (2006) Dynamic broadening of the crystal–fluid interface of colloidal hard spheres. *Phys Rev Lett* 97:228301.
7. Chacón E, Tarazona P, González LE (2006) Intrinsic structure of the free liquid surface of an alkali metal. *Phys Rev B* 74:224201.
8. Laird BB, Davidchack RL (2005) Direct calculation of the crystal–melt interfacial free energy via molecular dynamics computer simulation. *J Phys Chem B* 109:17802–17812.
9. Davidchack RL, Laird BB (2005) Crystal structure and interaction dependence of the crystal-melt interfacial free energy. *Phys Rev Lett* 94:086102.
10. Broughton JQ, Gilmer GH (1986) Molecular dynamics of the crystal–fluid interface. v. structure and dynamics of crystal–melt systems. *J Chem Phys* 84:5749–5758.
11. Huitema HEA, Vlot MJ, van der Eerden JP (1999) Simulations of crystal growth from Lennard-Jones melt: Detailed measurements of the interface structure. *J Chem Phys* 111:4714–4723.
12. Gasser U, Weeks ER, Schofield A, Pusey PN, Weitz DA (2001) Real-space imaging of nucleation and growth in colloidal crystallization. *Science* 292:258–262.
13. Pusey PN, van Megen W (1986) Phase behaviour of concentrated suspensions of nearly hard colloidal spheres. *Nature* 320:340–342.
14. Ackerson BJ, Schätzel K (1995) Classical growth of hard-sphere colloidal crystals. *Phys Rev E* 52:6448–6460.
15. Prasad V, Semwogerere D, Weeks ER (2007) Confocal microscopy of colloids. *J Phys Cond Matter* 19:113102.
16. Hoyt JJ, Asta M, Karma A (2001) Method for computing the anisotropy of the solid-liquid interfacial free energy. *Phys Rev Lett* 86:5530–5533.
17. Steinhardt PJ, Nelson DR, Ronchetti M (1983) Bond-orientational order in liquids and glasses. *Phys Rev B* 28:784–805.
18. Rein ten Wolde P, Ruiz-Montero MJ, Frenkel D (1996) Numerical calculation of the rate of crystal nucleation in a Lennard-Jones system at moderate undercooling. *J Chem Phys* 104:9932–9947.
19. Du D, Zhang H, Srolovitz DJ (2007) Properties and determination of the interface stiffness. *Acta Mater* 55:467–471.
20. Jeng US, Esibov L, Crow L, Steyerl A (1998) Viscosity effect on capillary waves at liquid interfaces. *J Phys Cond Matt* 10:4955–4962.
21. Penfold J (2001) The structure of the surface of pure liquids. *Rep Prog Phys* 64:777–814.
22. Harland JL, van Megen W (1997) Crystallization kinetics of suspensions of hard colloidal spheres. *Phys Rev E* 55:3054–3067.
23. Auer S, Frenkel D (2001) Prediction of absolute crystal-nucleation rate in hard-sphere colloids. *Nature* 409:1020–1023.
24. Warshavsky VB, Song X (2006) Fundamental-measure density functional theory study of the crystal-melt interface of the hard sphere system. *Phys Rev E* 73:031110.
25. Cheng Z, Zhu J, Chaikin PM, Phan SE, Russel WB (2002) Nature of the divergence in low shear viscosity of colloidal hard-sphere dispersions. *Phys Rev E* 65:041405.
26. Weeks ER, Weitz DA (2002) Properties of cage rearrangements observed near the colloidal glass transition. *Phys Rev Lett* 89:095704.
27. Dinsmore AD, Weeks ER, Prasad V, Levitt AC, Weitz DA (2001) Three-dimensional confocal microscopy of colloids. *App Optics* 40:4152–4159.
28. Yethiraj A, van Blaaderen A (2003) A colloidal model system with an interaction tunable from hard sphere to soft and dipolar. *Nature* 421:513–517.
29. Royall PC, Leunissen ME, Hynninen AP, Dijkstra M, van Blaaderen (2006) A re-entrant melting and freezing in a model system of charged colloids. *J Chem Phys* 124:244706.
30. Koehler SA, Hilgenfeldt S, Weeks ER, Stone HA (2004) Foam drainage on the microscale ii. Imaging flow through single plateau borders. *J Colloid Interface Sci* 276:439–449.
31. Crocker JC, Grier DG (1996) Methods of digital video microscopy for colloidal studies. *J Colloid Interface Sci* 179:298–310.

Hernández-Guzmán and Weeks